

# Williamson–Hall based X-ray peak analysis of a magnesium doped nano-hydroxyapatite powder produced by a combined ultrasonic and microwave heating-based method

Supriya Rattan, Derek Fawcett, Gerrard Eddy Jai Poinern

(Murdoch Applied Nanotechnology Research Group, Department of Physics, Energy Studies and Nanotechnology, Murdoch University, Australia)

---

**Abstract:** The present study used a combined ultrasonic and microwave heating-based method to produce pure and magnesium doped nano-hydroxyapatite powders. The powders were characterized using X-ray diffraction, Fourier transform infrared spectroscopy and field emission scanning electron microscopy. The Williamson-Hall (W-H) analysis techniques were used to study the effects of peak broadening in X-ray diffraction data. The analysis revealed magnesium ions were incorporated into the hydroxyapatite structure and changed the lattice parameters. The substitution of magnesium ions increased the (a) lattice parameter by (0.0689%) and slightly decreasing the (c) parameter by (0.2732%). The analysis also revealed magnesium substitution decreased the crystallite size, while properties like lattice strain, stress and anisotropic energy density were increased. Further, the presence of magnesium in the powders reduced their calcium content and acted as a growth inhibitor that that decreased crystallinity.

**Keywords:** Hydroxyapatite, ionic substitution, ultrasonic synthesis, X-ray peak analysis.

---

## 1. Introduction

Several members of the calcium orthophosphate family, with Ca/P molar ratios ranging from 0.5 to 2.0, have been extensively used in orthopedic and dental applications [1, 2]. Among the calcium orthophosphates, hydroxyapatite [HAP:  $\text{Ca}_{10}(\text{PO}_4)_6(\text{OH})_2$ ], with a similar chemical composition to the main inorganic component found in the mineral phase of natural bone is the most widely used [3]. Its widespread use is due to its good biocompatibility, its slow *in situ* biodegradability and its good osteoconductivity towards bone cells and other cellular tissues [4, 5]. However, biological forms of hydroxyapatite are nonstoichiometric and also contain small amounts of materials like fluoride, magnesium, potassium and sulphate. Because of this natural doping phenomena researchers have focused on manufacturing synthetic HAP-based materials doped with small concentrations of metallic ion additives like: silver (Ag); copper (Cu); zinc (Zn); iron (Fe), and magnesium (Mg) [6]. The inclusion of small concentrations of metallic ion additives do tend to modify the crystallographic properties without major changes to the hydroxyapatites hexagonal crystal structure [7]. However, these additives do influence hydroxyapatite's physiochemical properties (i.e. dissolution rate, solubility and surface chemistry), biological activity and interactions with surrounding tissues under physiological conditions [8]. Importantly, Mg is an important trace element found in calcified-tissues like bone (0.72 % by wt.), dentin (1.23% by wt.) and enamel (0.45% by wt.) [9]. And studies have that shown Mg acts like a growth factor during the early stages of osteogenesis, where the Mg ions promote alkaline phosphatase (ALP) activity, the growth of osteoblasts and the growth of bone mesenchymal stem cells [10, 11]. Mg is also actively involved in bone mineral metabolism pathways and calcification [12]. Thus, highlighting the importance Mg for promoting good bone health, and like the presence of calcium in bone, it also lowers the risk of osteoporosis [13]. Thus, the addition of small concentrations of Mg ions to HAP-based materials designed for orthopedic and dental applications is highly desirable for promoting positive biological activity and integration.

Because of the important beneficial effects of Mg in bone formation and calcification, new and efficient methods for producing Mg doped HAP-based materials for biomedical applications is highly desirable. Importantly, nanotechnology-based techniques have the ability to create new functional nanometer scale materials with unique properties that are significantly different from their conventional bulk counterparts [14, 15]. The present work uses nanotechnology-based principles to produce Mg doped nano-HAP powders suitable for biomedical applications. The synthesis process combines a sonochemical step that forms the Mg doped nano-HAP slurry, followed by the second microwave heating step. After which the raw powder undergoes a grinding step that produces the ultrafine powder. Sonochemical processing has the advantage of producing an acoustic cavitation effect, which generates the formation and subsequent collapse of bubbles within a liquid medium. The collapsing bubbles generate extreme reaction conditions, which produce extremely high temperatures (~5000 K) and high pressures (~20 MPa). Under these conditions it is possible to generate novel

nanomaterials with unique and distinctive physiochemical properties [16]. While microwave heating has the feature of volumetrically generating energy throughout the material, which is fundamentally different from thermal conduction that normally occurs in a conventional furnace [17]. After synthesizing the Mg doped nano-HAP powders, field emission scanning electron microscopy (FESEM) images were used to evaluate both mean particle size and morphology. In addition, X-ray diffraction (XRD) spectroscopy was carried out on the powder samples, and the resulting diffraction patterns were used to study the effects of peak broadening using Williamson-Hall (W-H) analysis. The analysis procedure used three evaluation methods: 1) uniform deformation model (UDM); 2) uniform stress deformation model (USDM), and 3) uniform deformation energy density model (UDEDM). From the analysis methods physical parameters like crystallite size, lattice strain, crystallite surface stress and energy density were determined.

## **2. Materials and methods**

### **2.1. Materials**

All chemicals used in preparing the samples were supplied by Chem. Supply Pty Ltd (Gillman, South Australia, Australia) and Sigma Aldrich (United States of America). All aqueous-based solutions were prepared using Milli-Q® water ( $18.3 \text{ M } \Omega \text{ cm}^{-1}$ ) produced by an ultrapure water system (Barnstead Ultrapure Water System D11931) supplied by Thermo Scientific Australia.

### **2.2. Methods**

#### **2.2.1. Preparation of pure nano-HAP and Mg doped nano-HAP powders**

Formulation of the pure nano-HAP powder started by pouring a 40 mL solution of 0.32M  $\text{Ca}(\text{NO}_3)_2 \cdot 4\text{H}_2\text{O}$  into a small glass beaker. The solution was then subjected to ultrasonic processing for 1 hour at maximum amplitude and operating at 400 W. The processor used was a UP400S supplied by Hielscher Ultrasound Technology (Teltow, Germany) and fitted with a 22 mm diameter Sonotrode operating at 24 kHz. During the hour, solution pH was maintained at 9 using 5 mL of  $\text{NH}_4\text{OH}$ . At the end of the first hour a 60 mL solution of 0.19M  $[\text{KH}_2\text{PO}_4]$  was added drop-wise to the solution during the second hour of processing. While solution pH was sustained at 9 and the Ca/P ratio of 1.67 was maintained. After processing the mixture underwent centrifugation ( $\sim 2000 \text{ g}$ ) which generated a precipitate. The Mg doped HAP powder was synthesized in the manner described above, except for the drop-wise addition of a 4ml solution of 0.16M  $\text{MgN}_2\text{O}_6$  in parallel with the abovementioned  $\text{KH}_2\text{PO}_4$ . The respective precipitates were collected and then individually subjected to microwave heating. The heating treatment was carried out in a microwave oven (Model TMOSS25, operated at 900 W at 2450 MHz and 240V and 50Hz) at full power for a 10 minute period. After heat treatment, the samples were individually ground to the consistency of an ultrafine powder using mortar and pestle. All powders were then studied using advanced characterization techniques.

#### **2.2.2. Powder characterization**

Preliminary particle size and shape analysis was undertaken using a JEOL JCM-6000, NeoScope™ electron microscope. Before imaging, samples were dried and then deposited onto carbon adhesive tape covered holders. Samples were then sputter coated (Cressington 208HR) with a 2 nm layer of platinum to prevent charge build up. In addition, elemental analysis of each sample was carried out using the energy dispersive spectroscopy (EDS) attachment of the microscope. High resolution images of the samples was carried out using a field emission scanning electron microscope (FESEM: FEI-Verios 460) operating at 5 kV, with 0.10 nA current and operating under secondary electron mode (Microscopy Centre at University of Western Australia). Functional groups and various vibrational modes present in the samples was identified by Fourier transform infrared spectroscopy (FT-IR). A PerkinElmer FT-IR / NIR Spectrometer Frontier fitted with a universal signal bounce Diamond ATR attachment was used to collect spectra. The spectra were recorded over the wavenumber interval ranging from  $400$  to  $4000 \text{ cm}^{-1}$  with a resolution step of  $1 \text{ cm}^{-1}$ . X-Ray Diffraction (XRD) spectroscopy analysis was undertaken with a GBC® eMMA X-Ray Powder Diffractometer ( $\text{Cu K}\alpha = 1.54056 \text{ \AA}$  radiation source) operating at 35 kV and 28 mA. The diffraction patterns were recorded over a  $2\theta$  range starting at  $10^\circ$  and ending at  $80^\circ$ . The incremental step size over the  $2\theta$  range was  $0.02^\circ$  and an acquisition speed used was  $2^\circ \text{ min}^{-1}$ . Analysis of the XRD patterns determined the position of the Bragg peaks and assisted with their identification using the ICDD (International Centre for Diffraction Data) and JCPDS (Joint Committee on Powder Diffraction Standards) databases. After identifying the Miller indices, peak broadening analysis was carried out using Williamson-Hall (W-H) methods to determine crystalline parameters like size, strain, stress and energy density.

### 3. Results and discussions

#### 3.1. X-ray peak investigation using Williamson–Hall analysis

Representative XRD patterns for a pure nano-HAP powder and Mg doped nano-HAP powder are presented in Fig. 1. Both patterns display several diffraction peaks that are characteristic of polycrystalline materials. The respective peak positions were identified and indexed according to the Joint Committee on Powder Diffraction Standards for pure hexagonal crystalline hydroxyapatite (JCPDS No. 09–0432). Miller indices were assigned to all significant peaks, as seen in Fig 1. Both diffraction patterns are similar, but the Mg doped sample has slightly sharper peak characteristics that indicate ionic substitutions have taken place. A similar result was reported by Kavitha *et al.* for ionic substitutions into HAP lattice structures [18]. In addition, elemental analysis carried out by EDS also confirmed the presence of Mg (1.14 atomic %) in the doped nano-HAP samples. The XRD analysis also failed to detect the presence of impurities in the powder samples. If any impurities were present in the samples they were below the detection limit.

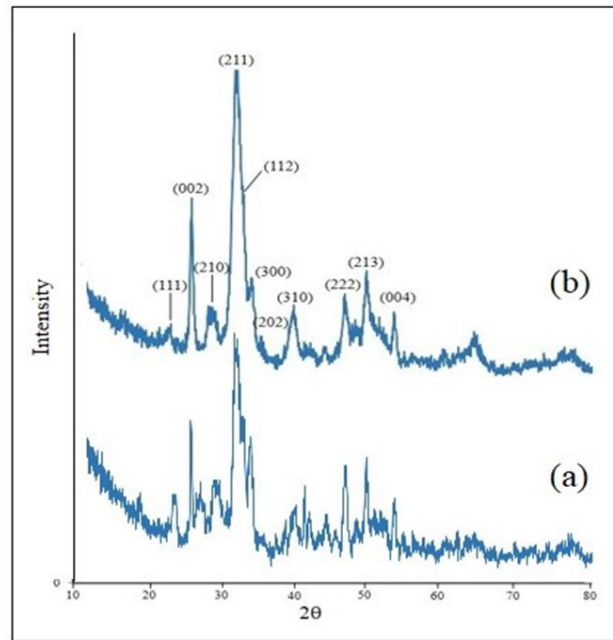


**Figure 1.** XRD patterns of sample powders: (a) pure nano-HAP and (b) Mg doped nano-HAP

The XRD data was then used to determine crystallite size using both the Scherrer ( $D_{s(hkl)}$ ) equation (1) and Williamson-Hall ( $D_{(hkl)}$ ) equation (2). Furthermore, Williamson-Hall analysis was also used to determine lattice strain ( $\epsilon$ ), crystalline stress ( $\sigma$ ) and anisotropic energy density ( $u$ ):

$$D_{s(hkl)} = \frac{k\lambda}{\beta_{(hkl)} \cos \theta_{(hkl)}} \quad (1)$$

$$\beta_{(hkl)} \cos \theta = \frac{k\lambda}{D_{(hkl)}} + 4\epsilon \sin \theta \quad (2)$$

Where  $\lambda$  is the wavelength of the monochromatic X-ray beam and crystallite shape constant  $k$ , which is 0.9 for spherical crystals with cubic unit cells. And  $\beta$  is the Full Width at Half Maximum (FWHM) of the peak at the maximum intensity,  $\theta_{(hkl)}$  is the peak diffraction angle that satisfies Bragg's law for the  $(h k l)$  plane,  $\epsilon$  is strain experienced by the lattice and  $D_{s(hkl)}$  and  $D_{(hkl)}$  are the respective crystallite sizes. The Williamson-Hall formulation presented in equation (2) represents the uniform deformation model (UDM). The model assumes uniform strain in all crystallographic directions and material properties are independent of direction within the crystal structure. Therefore, plotting  $4 \sin \theta$  along the x-axis and  $\beta_{(hkl)} \cos \theta$  along the y-axis enables the determination of slope ( $\epsilon$ ) and the (y-intercept) which aids in the determination of the crystallite size ( $D_{(hkl)}$ ). Plots of the pure nano-HAP and Mg doped nano-HAP powders is presented in Fig. 2 and the derived ( $D_{(hkl)}$ ) and  $\epsilon$  values are presented in Table 1.

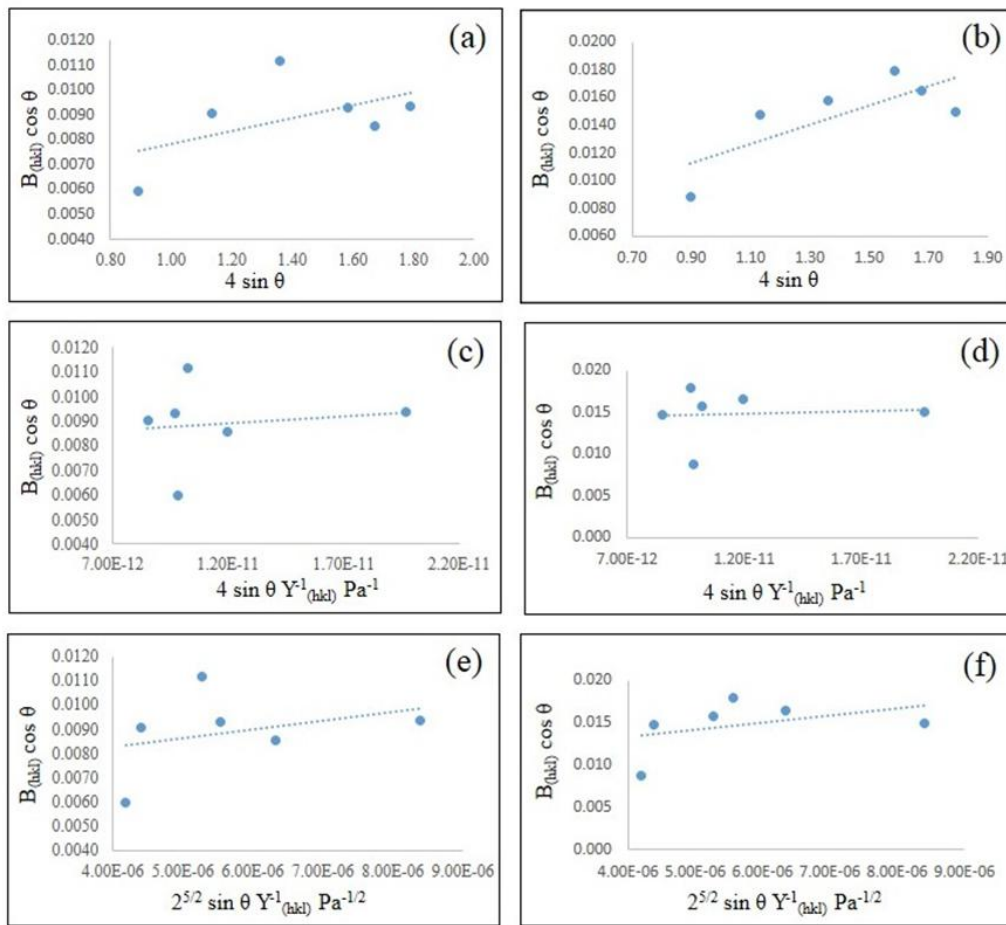


**Figure 2.**  $\beta_{(hkl)} \cos \theta$  versus  $4 \sin \theta$ ;  $\beta_{(hkl)} \cos \theta$  versus  $4 \sin \theta / Y_{(hkl)}$  and  $\beta_{(hkl)} \cos \theta$  versus  $4 \sin \theta (2u / Y_{(hkl)})^{1/2}$  for pure nano-HAP (a, c, e) and Mg doped nano-HAP (b, d, f) powder samples

Crystallite surface stress was estimated using the Uniform Stress Deformation Mode (USDM). The model assumes linear proportionality between stress and strain, or Hooke's law:

$$Y = \frac{\sigma}{\epsilon} \quad (3)$$

When the modulus of elasticity ( $Y_{(hkl)}$ ) or Young's modulus is substituted into equation (2) and rearranged it gives equation (4) below:

$$\beta_{(hkl)} \cos \theta = \frac{k\lambda}{D_{(hkl)}} + \frac{4\sigma \sin \theta}{Y_{(hkl)}} \quad (4)$$

In hexagonal crystallites like hydroxyapatite the elastic modulus  $Y_{(hkl)}$  is dependent on the crystallographic direction and is expressed by equation (5):

$$Y_{hkl} = \left( \frac{\left[ h^2 + \frac{(h+2k)^2}{3} + \frac{(al)^2}{c} \right]^2}{S_{11} \left( h^2 + \frac{(h+2k)^2}{3} \right)^2 + S_{33} \left( \frac{al}{c} \right)^4 + (2S_{13} + S_{44}) \left( h^2 + \frac{(h+2k)^2}{3} \right) \left( \frac{al}{c} \right)^2} \right) \quad (5)$$

The elastic compliances for the respective crystallographic directions are  $S_{11} = 7.49 \times 10^{-12}$ ,  $S_{33} = 10.9 \times 10^{-12}$ ,  $S_{44} = 15.1 \times 10^{-12}$  and  $S_{13} = -4.0 \times 10^{-12} \text{ m}^2 \text{ N}^{-1}$  [22]. Thus, plotting  $4 \sin \theta / Y_{(hkl)}$  along the x-axis and  $\beta_{(hkl)}$

cos  $\theta$  along the y-axis it is possible to determine the slope ( $\sigma$ ) and estimate crystallite size ( $D_{(hkl)}$ ) from the y intercept. The respective plots are presented in Figure 2 and the calculated ( $D_{(hkl)}$ ) and  $\sigma$  values are presented in Table 1.

**Table 1.** XRD peak analysis results for pure and Mg doped nano-HAP powders

Sample	Scherrer (002) (nm)	Williamson - Hall Methods					
		UDM		USDM		UEDDM	
		$D_{(hkl)}$ (nm)	$\epsilon \times 10^{-3}$	$D_{(hkl)}$ (nm)	$\sigma$ (M Pa)	$D_{(hkl)}$ (nm)	$u$ (KJ/m <sup>3</sup> )
Nano-HAP	24.37	25.85	2.473	17.84	52.17	20.25	18.96
Mg-nano HAP	15.67	17.62	6.941	9.89	66.79	13.7	28.64

The anisotropic energy density ( $u$ ) within the crystalline structure was estimated using the Uniform Deformation Energy Density Model (UEDDM). Thus, modifying equation (2) by substituting the strain energy for an elastic crystallite (Hooke's law) represented by equation (6) will give equation (7) below:

$$u = \frac{\epsilon^2 Y_{(hkl)}}{2} \tag{6}$$

$$\beta_{(hkl)} \cos \theta = \frac{k\lambda}{D_{(hkl)}} + 4 \sin \theta \left( \frac{2u}{Y_{(hkl)}} \right)^{\frac{1}{2}} \tag{7}$$

Thus plotting  $\beta_{(hkl)} \cos \theta$  along the y-axis and  $4 \sin \theta (2u/Y_{(hkl)})^{1/2}$  along the x axis, the anisotropic energy density  $u$  is determined from the slope and the crystallite size is determined from the y-intercept. The respective plots are illustrated in Fig. 2 and the calculated ( $D_{(hkl)}$ ) and  $u$  values are presented in Table 1.

The XRD data was also used to determine the lattice constants ( $a$ ,  $c$ ) and unit cell volumes ( $V$ ) of the samples using equations (8) and (9) respectively:

$$\frac{1}{d^2} = \frac{4}{3} \left( \frac{h^2 + hk + k^2}{a^2} \right) + \frac{l^2}{c^2} \tag{8}$$

$$V = \frac{\sqrt{3} a^2 c}{2} = 0.866 a^2 c \tag{9}$$

The calculated lattice constants and unit cell volumes are presented in Table 2.

**Table 2.** Lattice parameters & unit cell volume for pure and Mg doped nano-HAP powders

Sample	Lattice parameters		Unit cell volume
	$a$ (Å)	$c$ (Å)	$V$ (Å <sup>3</sup> )
Pure nano-HAP	9.4209	6.8819	528.946
Mg nano-HAP	9.4274	6.8631	528.229

Both Scherrer and Williamson-Hall analysis revealed a decrease in the crystallite size for the Mg doped nano-HAP powder compared to the pure nano-HAP powder as seen in Table 1. Similar studies have also reported a decrease in crystallite size with increasing concentrations of Mg doping in HAP-based powders [19, 20]. Also, a slight decrease in the unit cell volume (0.1356%) for the Mg doped nano-HAP powder sample was detected. In terms of the lattice parameters (Table 2), the substitution of Mg for Ca in the HAP lattice structure resulted in a slight increase in the ( $a$ ) parameter (0.0689%) and a significant decrease in the ( $c$ ) parameter (0.2732%). A similar study by Farzadi *et al.* has also reported similar changes in lattices parameters for doped HAP powders [21]. The change of size for both lattice parameters appears to be the consequence of Ca being replaced by Mg in the HAP structure. Importantly, the size difference between the ionic radius of Mg<sup>2+</sup> (0.065 nm) and the larger Ca<sup>2+</sup> (0.099 nm) results in distortions in the lattice structure and has also been found to lead to lower crystallinity [22, 23]. The lattice distortion created by Mg substitution also resulted in increases of  $\epsilon$ ,  $\sigma$  and  $u$  values as seen in Table 1. For instance, the lattice strain ( $\epsilon$ ) for the pure nano-HAP powder was  $2.473 \times 10^{-3}$ , while the Mg doped nano-HAP powder had the higher value of  $6.941 \times 10^{-3}$ . Similarly, there was also an

increase in surface stress ( $\sigma$ ) from 55.17 MPa for the pure nano-HAP sample to 66.79 MPa for the Mg doped sample, which equated to an increase in stress of around 21%. There was also an increase in energy density recorded for the Mg doped sample. In this case the pure nano-HAP sample had a value of 18.96 KJ/m<sup>3</sup>, while the Mg doped sample had the much higher value of 28.64KJ/m<sup>3</sup>. This equated to a 51% increase in the energy density.

FT-IR spectra for a pure and Mg doped nano-HAP powder samples is presented in Fig. 3. Starting from the right-hand side of both spectra, there is a wide and weak band located at 3432 cm<sup>-1</sup>, which is associated with adsorbed water in the nano-HAP lattice and corresponds to vibrations of OH<sup>-</sup> ions. The band in both samples is weak due to the microwave heat treatment which significantly reduces the presence of adsorbed water in their structures [24]. Further, the bands located at 1644 and 1384 cm<sup>-1</sup> are also weak in the pure nano-HAP sample and are due to the presence of carbonate ions produced during microwave heating. While in the Mg doped sample they only appear as slight traces. The stronger bands located at 1092 cm<sup>-1</sup>, 1032 cm<sup>-1</sup> and 961 cm<sup>-1</sup> correspond to the vibrational modes of the phosphate group (PO<sub>4</sub>)<sup>3-</sup>, which are typical for nano-HAP [25]. While the bands located at 564 cm<sup>-1</sup> and 601 cm<sup>-1</sup> are the result of O-P-O vibrational modes. The weaker 632 cm<sup>-1</sup> band indicates a hydroxyl vibrational mode and the band located at 832 cm<sup>-1</sup> indicates the presence of carbonates. The occurrence of carbonates in both samples arises from the interaction between atmospheric carbon dioxide and precursor's present in the alkaline reaction mixture. This phenomena has been reported in similar studies [26, 27]. Comparing the spectra reveals the pure nano-HAP sample has slightly sharper bands compared to the Mg doped sample. Thus indicating the addition of Mg into the HAP lattice structure leads to lower crystallinity. Similar metallic doping studies of HAP-based powders have also reported decreased crystallinity [28].

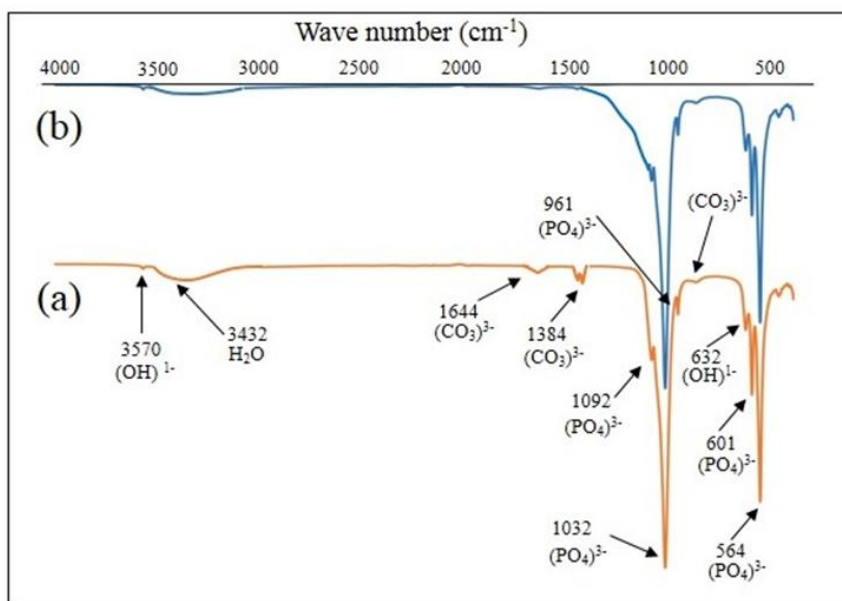


**Figure 3.** FTIR spectra: (a) pure nano-HAP and (b) Mg doped nano-HAP powders

The size and shape of nanoparticles present in the produced powders were investigated by analyzing images generated by FESEM. Representative images are presented in Fig. 4, with a pure nano-HAP powder sample being displayed in image (a) and an Mg doped nano-HAP powder sample being presented in image (b). Also presented in Fig. 4 are representative elemental analysis results of respective samples. The analysis of the pure nano-HAP powder (Fig. 4 (c)) revealed Ca (22.72 At. %) and P (13.46 At. %) were in close agreement to the ideal Ca/P ratio of 1.67. While the elemental analysis of the Mg doped nano-HAP powder (Fig. 4 (d)) revealed the Atom % for Ca had dropped slightly (21.58 At. %). Since Mg (1.14 At. %) was replacing Ca in the lattice structure. Image analysis revealed the pure nano-HAP powder particles were ellipsoid in shape with an average aspect ratio of around 1:7. Particle diameters ranged between 15 nm and 30 nm, while their lengths ranged between 80 nm to around 220 nm. The particles tended to cluster and form large agglomerations as seen in Fig. 4 (a). The images of the Mg doped sample revealed a different size range and shape as seen in Fig. 4 (b). These particles were predominantly granular in structure with a few scattered nano-rods. The granular particles ranged in size from 20 nm to 60 nm, while the few nano-rods were typically between 16 and 40 nm wide and around 80 to 140 nm long. The image analysis indicates the addition of Mg into the HAP structure hinders the

growth of the ellipsoid shaped crystallites. The smaller crystallite sizes seen in the XRD data and the FESEM images suggest that Mg doping acts as a growth inhibitor which inhibits the crystallization of HAP. Similar results have also reported increasing amounts of Mg causes lower levels of crystallinity [11, 29, and 30].

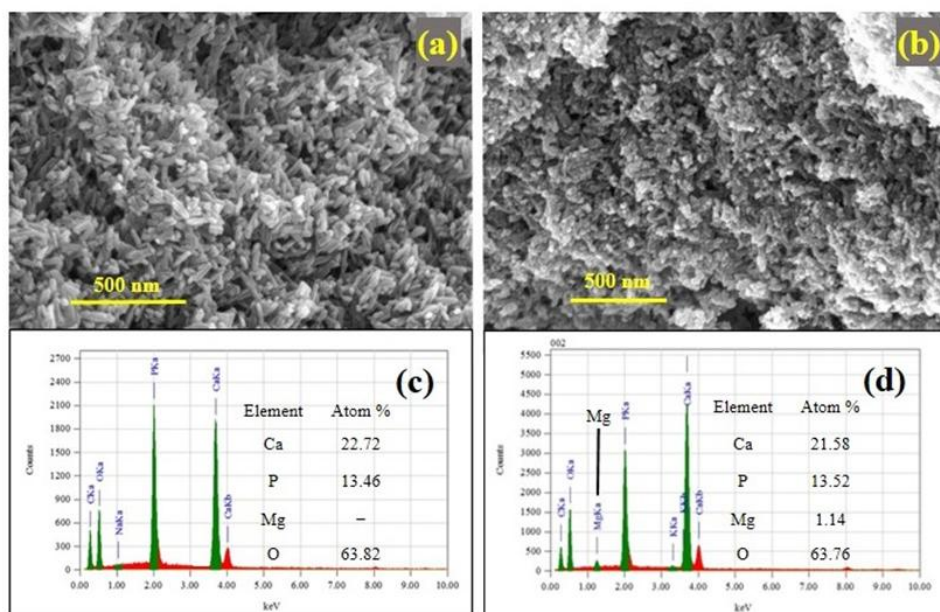


**Figure 4.** FESEM images: (a) pure nano-HAP powder & (b) Mg doped nano-HAP powder, Elemental analysis: (c) pure nano-HAP powder & (d) Mg doped nano-HAP

#### 4. Conclusion

Nano-HAP powders were prepared using a combined ultrasonic and microwave heating-based method. Both pure and Mg doped nano-HAP powders were successfully synthesized using this combined method. Analysis revealed Mg ions were incorporated into the HAP structure and resulted in small changes the lattice parameters. Mg substitution increased the (a) lattice parameter by (0.0689%) and slightly decreasing the (c) parameter by (0.2732%). The Williamson-Hall analysis revealed Mg substitution decreased crystallite size, while properties like stress and anisotropic energy density values increased by 21% and 51% respectively. Analysis also revealed Mg doping resulted in a decrease in calcium content of around 1.14 Atomic %. While FESEM studies of nanoparticle size and shape present in the Mg doped samples revealed the presence of Mg acted as a growth inhibitor and reduced the crystallinity of the resulting nano-HAP powder.

#### Conflict of interests

The authors declare that there is no conflict of interests regarding the publication of this manuscript.

#### Acknowledgements

Mrs. Supriya Rattan would like to acknowledge Murdoch University for providing her PhD Scholarship. The authors would also like to thank Centre for Microscopy, Characterization and Analysis, University of Western Australia for assistance with FESEM imaging.

#### References

- [1]. SV Dorozhkin, Calcium orthophosphates: occurrence, properties, bio-mineralization, pathological calcification and biomimetic applications, *Biomaterials*, 1(2), 2011, 121–164.
- [2]. DW Hutmacher, JT Schantz, CXF Lam, KC Tan, and TC Lim, State of the art and future directions of scaffold-based bone engineering from a biomaterials perspective. *J Tissue Eng. Regen. Med.*, 1, 2007 245–260.
- [3]. IN Sykaras, AM Iacopino, VA Marker, RG Triplett and RD Woody, Implant materials, designs, and surface topographies: their effect on osseointegration, a literature review. *The International Journal of Oral & Maxillofacial Implants*, 15, 2000, 675–690.
- [4]. LL Hench, Bioceramics: from concept to clinic, *J. Am. Ceram. Soc.*, 74, 1991, 1487–1510.
- [5]. GEJ Poinern, RK Brundavanam, P Nichols, M Cake, and D Fawcett, The characterization, mechanical properties and in vivo study of a porous ceramic derived from a 30 nm sized particle based powder of

- hydroxyapatite ceramics for potential hard tissue engineering applications, *Scientific Reports*, 4, 2014 6235: 1-9.
- [6]. MJ Robles-Aguila, JA Reyes-Avendano, and ME Mendoza, Structural analysis of metal-doped (Mn, Fe, Co, Ni, Cu, Zn) calcium hydroxyapatite synthesized by a sol-gel microwave-assisted method, *Ceram. Int.* 43, 2017, 12705–12709.
- [7]. S Kannan, and J Ferreira, Synthesis and thermal stability of hydroxyapatite- $\beta$ -tricalcium phosphate composites with co-substituted sodium, magnesium, and fluorine, *Chemical Materials*, 18(1), 2006, 198-203.
- [8]. J Kolmas, A Jaklewicz, A Zima, M Bucko, Z Paszkiewicz, J Lis, A Slosarczyk, and W Kolodziejski, Incorporation of carbonate and magnesium ions into synthetic hydroxyapatite: the effect on physical chemical properties, *J. Mol. Struct.*, 987(1–3), 2011, 40–50.
- [9]. SV Dorozhkin and M Epple, Biological and medical significance of calcium phosphates. *Angew. Chem.* 41, 2002, 3130–3146.
- [10]. D Laurencin, N Almora-Barrios, NH de Leeuw, C Gervais, C Bonhomme, F Mauri, W Chrzanowski, JC Knowles, RJ Newport, A Wong, Z Gan, and ME Smith, Magnesium incorporation into hydroxyapatite, *Biomaterials*, 32(7), 2011, 1826–1837.
- [11]. E Landi, G Logroscino, L Proietti, A Tampieri, M Sandri, and S Sprio, Biomimetic Mg-substituted hydroxyapatite: from synthesis to in vivo behaviour. *J. Mater. Sci. Mater. Med.* 19(1), 2008, 239–247.
- [12]. S Bose, G Fielding, S Tarafder, and A Bandyopadhyay, Understanding of dopant induced osteogenesis and angiogenesis in calcium phosphate ceramics. *Trends Biotechnol.*, 31, 2013, 594–605.
- [13]. M Supova, Substituted hydroxyapatites for biomedical applications: a review, *Ceram. Int.* 41, 2015 9203–9231.
- [14]. M Okada, and T Furuzono, Hydroxylapatite nanoparticles: Fabrication methods and medical applications. *Sci. Technol. Adv. Mater.*, 13, 2012, 064103.
- [15]. H Zhou, and J Lee. Nanoscale hydroxyapatite particles for bone tissue engineering. *Acta Biomater.* 7 2011, 2769–2781.
- [16]. A Gedanken, Using sonochemistry for the fabrication of nanomaterials, *Ultrason. Sonochem.*, 11, 2007; 47–55.
- [17]. M Vollmer. Physics of the microwave oven. *Phys. Ed.* 39(1), 2004, 74–81.
- [18]. M Kavitha, R Subramanian, KS Vinoth, R Narayanan, G Venkatesh, and N Esakkiraja, Optimization of process parameters for solution combustion synthesis of Strontium substituted Hydroxyapatite nanocrystals using Design of Experiments approach. *Powder Technol.*, 271, 2015, 167–181.
- [19]. Z Zhao, M Espanol, J Guillem-Marti, D Kempf, A Diez-Escudero, and MP Ginebra, Ion-doping as a strategy to modulate hydroxyapatite nanoparticle internalization, *Nanoscale*, 8, 2016, 1595–1607.
- [20]. O Kaygili, S Keser, N Bulut, and T Ates, Characterization of Mg-containing hydroxyapatites synthesized by combustion method, *Physica B: Condensed Matter*, 537, 2018, 63–67.
- [21]. A Farzadi, F Bakhshi, M Solati-Hashjin, M Asadi-Eydivand, and NAA Osman, Magnesium incorporated hydroxyapatite: synthesis and structural properties characterization, *Ceram. Int.* 40, 2014, 6021–6029.
- [22]. A Bigi, G Falini, E Foresti, M Gazzano, A Ripamonti, and N Roveri, Magnesium influence on hydroxyapatite crystallization. *J. Inorg. Biochem.* 49, 1993, 69–78.
- [23]. E Boanini, M Gazzano, and A Bigi, Ionic substitutions in calcium phosphates synthesized at low temperature, *Acta Biomater.* 6, 2010, 1882–1894.
- [24]. G Liangzhi, Z Weibin, and S Yuhui, Magnesium substituted hydroxyapatite whiskers: synthesis, characterization and bioactivity evaluation, *RSC Adv.*, 115, 2016, 114707–114713.
- [25]. X Lijuan, J Liyun, J Lixin, et al. Synthesis of Mg-substituted hydroxyapatite nanopowders: effect of two different magnesium sources, *Mater. Lett.* 106, 2013, 246–249.
- [26]. YJ Wang, JD Chen, K Wei, SH Zhang, and XD Wang, Surfactant-assisted synthesis of hydroxyapatite particles. *Mater Lett*, 60, 2006, 3227–3231.
- [27]. EL Beckett, NS Lawrence, YC Tsai, J Davis, and RG Compton, Bioanalytical utility of sonovoltammetry. *J Pharm Biomed Analysis*, 26(5–6), 2001, 995–1001.
- [28]. O Kaygili, and S Keser, Zr/Mg, Zr/Sr and Zr/Zn co-doped hydroxyapatites: synthesis and characterization, *Ceram. Int.*, 42, 2016, 9270–9273.
- [29]. H Zhang, C Zhao, J Wen, X Li, and L Fu, Synthesis and structural characteristics of magnesium and zinc doped hydroxyapatite whiskers. *Ceramics*, 61 (3), 2017, 244–249.
- [30]. J Ran, P Jiang, G Sun, Z Ma, J Hu, X Shen, and H Tong, Comparisons among Mg, Zn, Sr, and Si doped nano-hydroxyapatite/chitosan composites for load-bearing bone tissue engineering applications. *Mater. Chem. Front*, 1, 2017, 900-910.
-